

DISK-LOSS AND DISK-RENEWAL PHASES IN CLASSICAL BE STARS. II. CONTRASTING WITH STABLE AND VARIABLE DISKS

ZACHARY H. DRAPER^{1,2}, JOHN P. WISNIEWSKI³, KAREN S. BJORKMAN⁴, MARILYN R. MEADE⁵, XAVIER HAUBOIS^{6,7}, BRUNO C. MOTA⁶, ALEX C. CARCIOFI⁶, JON E. BJORKMAN⁴

Accepted in ApJ

ABSTRACT

Recent observational and theoretical studies of classical Be stars have established the utility of polarization color diagrams (PCD) in helping to constrain the time-dependent mass decretion rates of these systems. We expand on our pilot observational study of this phenomenon, and report the detailed analysis of a long-term (1989-2004) spectropolarimetric survey of 9 additional classical Be stars, including systems exhibiting evidence of partial disk-loss/disk-growth episodes as well as systems exhibiting long-term stable disks. After carefully characterizing and removing the interstellar polarization along the line of sight to each of these targets, we analyze their intrinsic polarization behavior. We find that many steady-state Be disks pause at the top of the PCD, as predicted by theory. We also observe sharp declines in the Balmer jump polarization for later spectral type, near edge-on steady-state disks, again as recently predicted by theory, likely caused when the base density of the disk is very high, and the outer region of the edge-on disk starts to self absorb a significant number of Balmer jump photons. The intrinsic *V*-band polarization and polarization position angle of γ Cas exhibits variations that seem to phase with the orbital period of a known one-armed density structure in this disk, similar to the theoretical predictions of Halonen & Jones. We also observe stochastic jumps in the intrinsic polarization across the Balmer jump of several known Be+sdO systems, and speculate that the thermal inflation of part of the outer region of these disks could be responsible for producing this observational phenomenon. Finally, we estimate the base densities of this sample of stars to be between $\approx 8 \times 10^{-11}$ to $\approx 4 \times 10^{-12}$ gcm⁻³ during quasi steady state periods given their maximum observed polarization.

Subject headings: circumstellar matter — stars: individual (pi Aquarii, 60 Cygni, 48 Librae, psi Persei, phi Persei, 28 Cygni, 66 Ophiuchi, gamma Casseopia, omega Orionis, FY CMA, 59 Cyg)

1. INTRODUCTION

Classical Be stars are a subset of B-type main sequence stars which are characterized by their rapid rotational velocities ranging from 60% to 100% of their critical rate (Rivinius, Carciofi, & Martayan 2013). They have a geometrically flattened decretion disk that is fed from material from the stellar photosphere as diagnosed from studies of their optical/IR emission lines, polarization, and interferometric signatures (see e.g. Porter & Rivinius 2003; Stee 2011). A large volume of observations suggest the kinematic properties of these gas disks is best represented by near Keplerian rota-

tion (Hummel & Vrancken 2000; Meilland et al. 2007a; Pott et al. 2010; Wheelwright et al. 2012; Kraus et al. 2012). For the most up to date review of Classical Be stars see Rivinius, Carciofi, & Martayan (2013).

As summarized in Carciofi et al. (2011), the viscous decretion disk model developed by Lee et al. (1991) can explain many of the observational signatures of Be disks, although other models have been explored to explain the structure of these disks (Bjorkman & Cassinelli 1993; Cassinelli et al. 2002; Brown et al. 2008). One key unanswered question in the study of Be disks is what mechanism(s) are responsible for injecting material into these disks. Non-radial pulsations have been suggested to be one contributing factor to supplying material to some of these disks (Cranmer 2009; Rivinius et al. 1998; Neiner et al. 2002), while periastron passage of binary companions may contribute in other systems such as δ Scorpii (Miroshnichenko et al. 2001, 2003). This scenario for δ Scorpii is now questionable given the disk's growth prior to the periastron passage of 2011 (Miroshnichenko et al. 2013). Nonetheless, binarity may play a role in the phenomenon and disk variability. For example, the source of material and angular momentum in non-classical Be stars can be the result of a red giant phase binary transferring material to create a Be+sdO system Gies et al. (1998). Characterizing the evolution of Be stars' mass-loss rates is another promising approach to constrain the disk-

¹Department of Physics and Astronomy, University of Victoria, 3800 Finnerty Rd, Victoria, BC V8P 5C2 Canada

²Herzberg Institute of Astrophysics, National Research Council of Canada, Victoria, BC V9E 2E7 Canada

³HL Dodge Department of Physics & Astronomy, University of Oklahoma, 440 W Brooks St, Norman, OK 73019 USA, wisniewski@ou.edu

⁴Ritter Observatory, Department of Physics & Astronomy, Mail Stop 113, University of Toledo, Toledo, OH 43606 USA, karen.bjorkman@utoledo.edu, jon@physics.utoledo.edu

⁵Space Astronomy Lab, University of Wisconsin-Madison, 1150 University Avenue, Madison, WI 53706 USA, meade@astro.wisc.edu

⁶Instituto de Astronomia, Geofísica e Ciências Atmosféricas, Universitária de São Paulo, Rua do Matão 1226, Cidade Universitária, 05508-900 São Paulo, SP Brazil, xhaubois@astro.iag.usp.br, carciofi@usp.br

⁷Sydney Institute for Astronomy, School of Physics, University of Sydney, NSW 2006, Australia

feeding mechanism. On short time-scales, Carciofi et al. (2007) noted polarimetric variability in Arcturus likely arising from injections of discrete blobs of mass into the inner disk, that subsequently circularize into rings. Studying longer duration disk-loss and disk-regeneration events (Underhill & Doazan 1982; Doazan et al. 1983; Clark et al. 2003; Vinicius et al. 2006; Haubois et al. 2012), including the time-scales (Wisniewski et al. 2010) and statistical frequency (McSwain et al. 2008, 2009) of these episodes, is another way to diagnose the mechanism feeding Be disks.

Polarimetry has been used to study the Be phenomenon for both individual Be stars (Quirrenbach et al. 1997; Wood et al. 1997; Clarke & Bjorkman 1998) and larger statistical surveys (Coyne & Kruszewski 1969; McLean & Brown 1978; Poeckert et al. 1979; Wisniewski et al. 2007b). It is widely believed that Thompson scattering (free-electron scattering) is the source of polarization in Be stars (Wood et al. 1996a,b; Halonen et al. 2013). Pre- or post-scattering absorption of photons within the disk can imprint wavelength dependent signature on top of the wavelength independent Thompson scattering (Wood & Bjorkman 1995). Because the polarization across the Balmer jump traces material in the innermost regions of disks ($\sim 6 R_*$; Carciofi et al. 2011, Halonen & Jones 2013a) and the V -band polarization is a tracer of the total scattering mass of the disk, studying the time evolution of the wavelength-dependence of polarization in Be stars can be used to constrain the time dependence of the mass accretion rate and the α parameter in these systems. Specifically, the slope, shape, and temporal evolution of polarization color diagrams (PCD) observed in Be systems (Draper et al. 2011) have been theoretically reproduced, for the first time, by time-dependent radiative transfer models in which the mass accretion rate, α parameter, and inclination angle are the primary variables (Haubois et al. 2013). In addition to density changes caused by changes in the mass accretion rate, it has been suggested that PCD diagram loops can also be produced by one-armed density perturbations (Halonen & Jones 2013b).

In this paper, we implement the PCD diagram diagnostic developed in Draper et al. (2011) on a broader sample of Be stars, including systems showing evidence of experiencing disk-loss events and those whose disks appear roughly stable over time. We describe the data sample in Section 2, and discuss the techniques we used to remove the interstellar polarization component from each dataset in Section 3. We discuss the temporal evolution of each Be disk in PCD diagram parameter space in Section 4, and also detail evidence of variability in the disk position angle in select systems. Finally, we summarize the major results of this manuscript in Section 5.

2. OBSERVATIONS AND DATA REDUCTION

The spectropolarimetric data analyzed in this study were obtained by the University of Wisconsin's (UW) HPOL spectropolarimeter, mounted on the 0.9m Pine Bluff Observatory (PBO) telescope. Data obtained before 1995 were recorded using a dual Reticon array detector spanning the wavelength range of 3200-7600Å with a spectral resolution of 25Å (Wolff et al. 1996). Beginning

in 1995, HPOL's detector was upgraded to a 400 x 1200 pixel CCD camera that provided coverage from 3200-6020Å at a resolution of 10Å and 5980-10,500Å at a resolution of 7Å (Nordsieck & Harris 1996). Further details about HPOL can be found in Nook (1990), Wolff et al. (1996), and Harries et al. (2000).

Data obtained by HPOL were reduced and calibrated using REDUCE, a spectropolarimetric software package developed by the University of Wisconsin-Madison (see Wolff et al. 1996). Routine monitoring of unpolarized standard stars at PBO has enabled the instrumental polarization to be carefully calibrated. The residual instrumental systematic errors depend mildly on the date of the observations, but range from 0.027-0.095% in the U -band, 0.005-0.020% in the V -band, and 0.007-0.022% in the I -band. At the current time, HPOL data from 1989 to 2000 are available on the STScI MAST archive⁸.

HPOL spectroscopic data were not flux calibrated to an absolute level because of nonphotometric skies typically present during the observations. To mitigate any relative flux offsets between red and blue grating data obtained on the same night, we applied a constant multiplicative factor to the grating with the lower flux in an observation, and then merged the red and blue grating bandpasses.

When available, HPOL observations were supplemented with observations from the Wisconsin Ultraviolet Photo-Polarimeter Experiment (WUPPE) from both the Astro-1 and Astro-2 missions flown on the Space Shuttles Columbia and Endeavor, respectively. WUPPE is a 0.5 meter telescope with a spectropolarimeter which simultaneously obtained spectra and polarization from 1500 to 3200Å with a resolution of about 16Å. For a more detailed explanation of the instrument see Nordsieck et al. (1994), and Clayton et al. (1997) for a detailed description of the pre-flight and in-flight calibrations.

Additional spectroscopic observations of 66 Oph obtained with the fiber-fed echelle spectrograph mounted on the Ritter Observatory 1m telescope were also analyzed. These observations were obtained with the default spectrograph setup, yielding $R \sim 26,000$. These data were reduced using standard IRAF techniques. A summary of the data used for each star in this study is in Table 1.

3. DATA ANALYSIS

3.1. Interstellar Polarization

Before any robust interpretations of polarization from our classical Be stars can be made, the interstellar polarization (hereafter, ISP) must be removed. The ISP is due to a dichroic scattering in the interstellar medium (hereafter, ISM) imprinting itself on the intrinsic polarization of the science target. There are three common techniques which are used to characterize the ISP: field stars, emission lines, and utilizing the wavelength dependence of the observed polarization. (Wisniewski et al. 2007a). In this paper, we take advantage of the field star and wavelength dependence to diagnose the ISP for our target stars and try to present an improved and streamlined process for determining ISP for spectropolarimetry from long surveys, like HPOL.

⁸ See archive website for more up to date details: <http://archive.stsci.edu/hpol/>

3.1.1. 48 Lib

Using our IDL routines, the calibrated HPOL data was processed in a manner similar to the ISP removal process in Quirrenbach et al. (1997) and Wisniewski et al. (2010) to constitute a standardized ISP determination process. We measure the raw Johnson V -band polarization measurements from the spectropolarimetry using equations 1 and 2,

$$\%P = \int_{\lambda_1}^{\lambda_2} \frac{P(\lambda) * F(\lambda) * w(\lambda)}{F(\lambda) * w(\lambda)} \quad (1)$$

$$\%P_{err} = \frac{1}{\sqrt{n}} \int_{\lambda_1}^{\lambda_2} d\lambda \frac{\text{Err}(\lambda) * F(\lambda) * w(\lambda)}{F(\lambda) * w(\lambda)} \quad (2)$$

where $P(\lambda)$ is a stokes parameter of the spectropolarimetry (Q , U , or P), $F(\lambda)$ is the relative flux, and $w(\lambda)$ is the filter function desired to weight the data. The error measurement is divided by a Poisson statistic, where n is the total number of data points within the wavelength range. This is consistent with the *pfil* command in the REDUCE software code developed for HPOL (Wood et al. 1996a). These raw V -band polarization data are compiled in Table 2 for every target in our sample.

When they are not spatially resolved, Be systems exhibit linear polarization along a single, preferred position angle, defined by the orientation of the disk's major axis on the sky. We fit a linear trend through the data in the QU plane to determine this mean disk polarization axis (Fig 1, left column). Then we rotated the entire data set by the mean intrinsic disk angle, thereby putting them into a rotated (Q' U') space. The ISP perpendicular component (P_{\perp}) to the intrinsic polarization, i.e. along the U' axis, in this regime is independent of the intrinsic disk polarization. The Q' axis is comprised of the parallel component of ISP (P_{\parallel}) plus the intrinsic disk polarization.

The U' axis for all observations were then combined with a error weighted mean (Fig 1, middle column). To extend the wavelength coverage of these data, which aids our effort to robustly model the wavelength dependent ISP signature described below, we supplemented our target stars with archival WUPPE data where possible (Table 1). These archival UV data were rotated by the same intrinsic disk angle determined for each star and merged with the optical U' spectropolarimetry. We then fit these U' data with a modified version of the empirical Serkowski law (Serkowski et al. 1975; Wilking et al. 1982),

$$P(\lambda) = P_{\perp} \exp[-K \ln^2(\lambda_{\max}/\lambda)] \quad (3)$$

$$K = (1.68 * 10^{-4}) * (\lambda_{\max}) - 0.002 \quad (4)$$

to determine the perpendicular component of ISP. λ_{\max} can be determined by the wavelength of the Serkowski curves' inflection point at the peak amplitude of ISP. This characteristic Serkowski profile stems from dichroic absorption of the ISM where certain wavelengths are preferentially scattered from dust grains aligned with the galactic magnetic field.

Following the methodology used in Quirrenbach et al. (1997), we compute the ISP_{\parallel} component by assuming

that the PA of the total ISP is sufficiently represented by nearby field stars to each of our targets, and then using simple geometry to extract the magnitude of the ISP_{\parallel} component. For each of our science targets, we generated a field star PA estimate (PA_{fs}) by selecting stars from the Heiles (2000) catalog in the vicinity of each science target (3 degree maximum separation and within 150 pc of the target) that exhibit no conspicuous intrinsic polarization (Table 3). We separated the V -band polarization for each field star into Q and U components, computed an error weighted mean, and finally used this error weighted mean to compute the final field star PA for each science target (Table 3). The error in this PA was computed using the standard deviation of QU :

$$PA = 0.5 * \tan^{-1} \left(\frac{U}{Q} \right) \quad (5)$$

$$PA_{err} = \frac{\sigma U * Q + \sigma Q * U}{U^2 + Q^2} \quad (6)$$

Given the amplitude of ISP_{\perp} and the field star PA, we compute the amplitude of ISP_{\parallel} using simple geometry:

$$P_{\parallel} = \frac{P_{\perp}}{\tan(2 * PA_{fs})} \quad (7)$$

Finally, the total ISP is computed using the amplitude of ISP_{\perp} and ISP_{\parallel} :

$$P_{ISP} = \sqrt{P_{\perp}^2 + P_{\parallel}^2} \quad (8)$$

With the P_{ISP} , λ_{\max} and PA_{fs} the ISP characterization is complete. As a check of the accuracy of our ISP removal, we plot the resultant intrinsic polarization on a Stokes QU diagram and confirm that the data pass through the origin (Fig. 1A, B, and C, right column) with 48 Lib shown in Fig. 1A. The final ISP values, along with the parallel and perpendicular components, are tabulated in Table 4 for each science star. For 48 Lib, our final ISP parameters of $P_{\max} = 0.86\%$ and $\theta = 93^{\circ}$ are consistent with the ISP PA derived from previous field star (82 ± 22) and $H\alpha$ line depolarization (85 ± 3) studies (Poeyckert et al. 1979) and amplitude of ISP derived from these studies (0.64% - 0.73%; Poeyckert et al. 1979). Removing this ISP component yields the time-dependent intrinsic polarization behavior within our data (Fig 2), which is compiled in Table 5 for all targets in our sample.

3.1.2. ϕ Per

When the intrinsic polarization angle was not well determined, the ISP removal process described in Section 3.1.1 failed, as diagnosed by the combined U' data set exhibiting a Balmer jump instead of a characteristic Serkowski curve. For ϕ Per this breakdown occurred because the source exhibited minimal variability in its intrinsic polarization levels, such that the raw data were not well fit by a linear trend on the QU diagram (see Fig 1a). To mitigate this, instead of using the V -band polarization to determine the intrinsic PA on the QU diagram we used the raw polarization data across the Balmer jump 3200-4000 Å. The differing opacity across the Balmer jump imprints a change in amplitude of linear polarization across the jump. Plotting the polariza-

tion across the Balmer jump in QU space helps to differentiate the intrinsic polarization of the disk, thereby allowing us to fit these data with a linear trend to derive the intrinsic disk position angle. Once the intrinsic disk PA was determined, we adopted the ISP PA of Quirrenbach et al. (1997) and determined the ISP parameters using the rest of the procedures described in Section 3.1.1. Our total ISP polarization, $P_{\max} = 0.76\%$, was similar to that found by Quirrenbach et al. (1997), 0.82% . The resultant time-dependent intrinsic polarization of ϕ Per is shown in Fig 2a and Table 5.

3.1.3. γ Cas

Like ϕ Per, the long-term stability of γ Cas's disk necessitated use of its polarization across the Balmer jump to characterize the intrinsic disk position angle (Fig 1a). We adopted the field star PA used by McLean & Brown (1978) and Quirrenbach et al. (1997) (see Table 4). The final ISP parameters we derived, $P_{\max} = 0.31\%$ and $\theta = 95^\circ$ (Table 4), were consistent with those derived by Quirrenbach et al. (1997), $P_{\max} = 0.26\%$ and $\theta = 95^\circ$. The time-dependent intrinsic polarization of γ Cas is shown in Fig 2a and Table 5.

3.1.4. 66 Oph

We adopted the same ISP method used for 48 Lib on 66 Oph. After defining the major axis of the disk by fitting a linear regression to the V -band polarization data plotted in a QU diagram (Fig 1b), we determined ISP_{\perp} by fitting a Serkowski law to the U' data and ISP_{\parallel} from the PA of nearby field stars (Table 3). The final ISP parameters we derived, $P_{\max} = 0.45\%$ and $\theta = 81^\circ$ (Table 4), were consistent with those derived by Poeckert et al. (1979) from field star and $H\alpha$ line depolarization, $P_{\max} = 0.51\text{-}0.52\%$ and $\theta = 82\pm 3 - 86\pm 19$. The time-dependent intrinsic polarization of 66 Oph is shown in Fig 2b and Table 5.

3.1.5. ω Ori

ω Ori exhibited significant V -band polarization variability, which enabled us to determine the PA of the disk's major axis by fitting a linear regression to these data in the Stokes QU diagram (Fig 1b). While we were able to determine ISP_{\perp} by fitting a Serkowski law to the U' data (middle panel, Fig 1b; Table 4), the field star PA estimates for this source varied from $20\text{-}165$ (Table 3), with an average value of $36\pm 9.7^\circ$. Previous estimates of the ISP towards ω Ori indicated that the magnitude of ISP was low ($<0.05\%$, Poeckert et al. 1979 to $\sim 0.1\%$, McLean & Brown 1978), and the orientation of this ISP ranged from 151° (Poeckert et al. 1979) to being undetermined (McLean & Brown 1978). Our long temporal baseline of spectropolarimetric data is particularly helpful in constraining the ISP PA as Figs. 1b and 2b indicate that ω Ori experienced disk depletion events. Because the variation in the raw V -band polarization (Fig 2) passes near the origin in QU space, this excludes our average field star PA (36°) from being a viable ISP PA. Furthermore, an adopted ISP PA of 36° would cause the V -band polarization and $H\alpha$ to have an anti-correlated trend with time. Rather the total ISP PA must lay in the third quadrant of the QU diagram ($90\text{-}135^\circ$). We estimate this PA to be $\sim 110^\circ$, under the assumption that

our lowest polarization data captures the system in a near disk-less state, akin to the scenario considered by Wisniewski et al. (2010). Removing our estimate of the total ISP, $P_{\max} = 0.23\%$ and $\theta = 110^\circ$, from these data yields the time-dependent intrinsic polarization shown in Fig. 2b and Table 5.

3.1.6. ψ Per

ψ Per exhibited significant variability in its total V -band polarization across the time sampling of our data (Fig 1b), enabling us to determine the PA of the disk's major axis. The perpendicular component of ISP was weak and poorly constrained by a Serkowski law (middle panel, Fig 1b). We adopted a field star PA of 112° , yielding final ISP parameters of $P_{\max} = 0.09\%$ and $\theta = 112^\circ$. These parameters are generally consistent with those determined by Poeckert et al. (1979) ($P_{\max} = 0.31\pm 0.11\% - 0.36\pm 0.10\%$; $\theta = 128\pm 13 - 129\pm 10$) and McLean & Brown (1978) ($P_{\max} = 0.4\%$ and $\theta = 135^\circ$). However, they are finding a stronger parallel ISP component. Removing this ISP yields the time-dependent intrinsic polarization shown in Fig. 2b and Table 5.

3.1.7. 28 Cyg

We determined the PA of the disk major axis of 28 Cyg by fitting the variation in its V -band polarization in the QU frame with a linear regression (Fig. 1c). Previous studies have suggested a weak ISP along the line of sight to 28 Cyg ($<0.20\%$, Poeckert et al. 1979; 0.1% , McLean & Brown 1978), which agrees with our new analysis. We found 28 Cyg had a very weak ISP_{\perp} component (Fig 1; Table 4). Based on a field star PA of 79° (Table 3), we determined final ISP parameters of $P_{\max} = 0.25\%$ and $\theta = 79^\circ$. Removing this small ISP component yielded the time-dependent intrinsic polarization shown in Fig. 2c and Table 5.

3.1.8. FY CMa

Both the raw V -band polarization (Fig 1c) and polarization across the Balmer jump were well fit with a linear regression passing near the origin. This unique situation presents substantial challenges for determining the ISP, as it either implies that the ISP component is zero or it implies that the ISP component is aligned with the intrinsic disk axis. In the latter scenario, one would only be able to robustly determine the ISP during epochs in which FY CMa experienced a complete loss of its disk (see e.g. Wisniewski et al. 2010). For the purposes of this paper we have assumed the ISP component is small ($P_{\max} = 0.04\%$ and $\theta = 136^\circ$). The nominal field star PA, 136° (Table 3), is $\sim 20^\circ$ from the PA of the disk major axis, which supports our assumption that the ISP towards FY CMa is not parallel with the intrinsic PA. The time-dependent intrinsic polarization for FY CMa is shown in Fig. 2c and Table 5.

3.1.9. 59 Cyg

Like ϕ Per and γ Cas, the long-term stability of 59 Cyg's V -band polarization (see Fig 1c) forced us to measure the change in polarization across the Balmer jump to characterize the intrinsic disk position angle. We were able to determine ISP_{\perp} by fitting a Serkowski law to the UV and optical U' data (Fig. 1c); however, the total

ISP PA suggested by field stars surrounding 59 Cyg ($29 \pm 35^\circ$; Table 3) is unlikely to be correct as this lays parallel to the intrinsic disk PA. This could only be plausible if the ISP_\perp was instead zero. We therefore were unable to determine a robust total ISP for 59 Cyg. As will be discussed in Section 4.5, we did explore the behavior of 59 Cyg’s mostly intrinsic polarization across the Balmer jump (Fig. 2c) assuming a total ISP around 0° . Specifically, we explored ISP parameter space about this adopted value and confirmed that, even though there is significant uncertainty in the correct total ISP PA, this did not specifically affect the observed Balmer jump polarization discussed in that section.

3.1.10. 60 Cyg and π Aqr

Wisniewski et al. (2010) already used the total disk loss phases of 60 Cyg and π Aqr to establish well determined ISP parameters for these systems. We applied the IDL code and basic techniques used throughout this paper on these data (see Figs. 1 and 2), and adopted the same total ISP PA as used in Wisniewski et al. (2010). This enabled us to test the effects of using different binning during the fitting process as compared to the earlier work (e.g. 60 Cyg) as well as the effects of including UV polarimetry and different binning (e.g. π Aqr). As seen in Table 4, the ISP parameters we derive are fully consistent with those reported in Wisniewski et al. (2010).

3.2. $H\alpha$ Equivalent Widths

To help assess the temporal behavior of the disk systems in our sample, we computed $H\alpha$ EWs from our spectropolarimetric data in the last column of Table 5. We processed HPOL flux data using IDL code that computed EWs using the trapezoid rule:

$$EW = \sum_{n=\lambda_1}^{\lambda_2} \left(1 - \frac{0.5 * (F(n)_{line} + F(n+1)_{line})}{F_{cont}} \right) \Delta\lambda \quad (9)$$

where F_{cont} is the continuum flux computed from 6366-6456 Å and 6666-6756 Å. The $H\alpha$ line flux was computed from 6516-6606 Å (λ_2 and λ_1).

Minor variations in $H\alpha$ EWs can be seen in HPOL data that span the change from a Reticon to a CCD detector in 1995. These variations are not considered real, but rather are likely due to the slight change in spectral resolution achieved between the two different instrument configurations (see Section 2). A small number of archival spectroscopic observations of 66 Oph (Table 6), obtained at Ritter Observatory, were also analyzed in this paper to supplement the HPOL data. As noted previously by Wisniewski et al. (2010), there is also a flux offset between $H\alpha$ EWs computed from HPOL and Ritter data, likely owing to the different resolutions of these data. Since we are merely interested in using these data to track the long-term evolution of 66 Oph, this offset does not affect our analysis or interpretations.

4. DISCUSSION

4.1. Additional Disk-Growth and Loss Phases

In paper I of this series, we analyzed well sampled, long-term spectropolarimetric data for two classical Be stars that clearly underwent a complete disk-loss phase. In this paper, we explore the behavior of a larger sample of classical Be stars, including systems that exhibit disks that are stable over time periods of more than a decade, as well as systems that exhibit at least partial disk-loss/disk-renewal phases. While detailed modeling of each system that exhibits a non-stable disk is clearly necessary and warranted, albeit outside the scope of this paper, we discuss some of the basic observational properties of these systems below.

4.1.1. ψ Per

The intrinsic polarization and $H\alpha$ EW of ψ Per both exhibit clear evidence of significant variability over the ~ 13 year time coverage of our data (Fig. 2b). Throughout the early 1990s, the steady increase in the system’s intrinsic polarization, lasting for ~ 1400 days, accompanied by a small strengthening in its $H\alpha$ EW is indicative of a growth in density and size of the disk. Although the data sampling is sparse, there is evidence that the disk generally stabilized in strength between 1995-2001. Figure 2b also exhibits a dramatic, monotonic drop in intrinsic polarization over a period of ~ 190 days starting in August 2002, along with a more gradual, time-delayed, significant decrease in $H\alpha$ EW. These trends are consistent with a major inside-out clearing of significant mass from the disk (Wisniewski et al. 2010). Since a small level of both intrinsic polarization and $H\alpha$ emission remained after the event, we characterize this as an incomplete disk-loss event.

Characterizing the time-scale of disk-loss events is important in order to constrain the viscosity parameter, α , assuming the disk dissipates on a viscous time-scale. Equation (19) of Bjorkman & Carciofi (2005) describes such an assumption and can be rewritten to give α as function of the diffusion timescale, t_{diff} .

$$\alpha = (0.2\text{yr}/t_{diff}) * (r/R_\star)^{0.5} \quad (10)$$

Assuming the bulk of the scattering events producing the observed polarization occurs at a radial distance of $\sim 5 R_\star$ and the (partial) disk-loss time-scale of ~ 190 days yields $\alpha \sim 0.86$ for ψ Per. This value is intermediate compared to estimates for 60 Cyg (~ 0.1 ; Wisniewski et al. 2010) and robustly measured for 28 CMa (1 ± 0.2 ; Carciofi et al. 2012). Because the ψ Per disk did not completely clear out, our quoted disk-loss time-scale is a lower limit and correspondingly the quoted α parameter is an upper limit. Clearly, characterizing the viscosity parameter for a larger number of systems is required to assess whether there is a preferred parameter for most Be disks.

4.1.2. ω Ori

The overall steady decline in $H\alpha$ EW strength throughout most of the 13 years of coverage in our dataset (Fig. 2b) is indicative of a gradual, albeit incomplete, loss of the system’s disk. The ~ 1500 day duration decline in intrinsic V-band polarization starting at the beginning of our dataset is consistent with a gradual loss of

the system’s disk. Mirroring the scenario observed in π Aqr reported by Wisniewski et al. (2010), the subsequent ~ 1100 day long increase in intrinsic polarization is likely responsible for the temporary halt in the decline of H α EW strength between 1995-1998 and indicative of temporary replenishment of material to the inner regions of the disk. The cessation of this mass injection to the inner disk is marked by a fast decrease in the intrinsic polarization level, as well as a resumption of the gradual decline in H α EW. Near the end of our dataset, the sharp rise in both intrinsic polarization and H α EW indicate significant mass injection into the disk. Overall, these disk-loss and growth epochs occurred in the span of 2-4 years.

4.1.3. 66 Oph

The H α EW of 66 Oph also exhibited a steady decline throughout the entire 13 year baseline of our dataset (Fig. 2b). Supplementary H α EWs from spectra obtained at Ritter Observatory improve the time sampling during the end of our spectropolarimetric data, and confirm that the emission strength decline continues during these epochs. The Ritter EWs end their decline after the last epoch of our spectropolarimetric data (see e.g. Table 6), suggesting the system’s mass-loss rate changed and a complete disk-loss phase was avoided. The intrinsic polarization data (Fig 2b) also exhibit a slow decline throughout the 13 year baseline of the HPOL data, supporting the interpretation of a gradual decline in the disk.

4.2. Intrinsic Polarization Color Diagrams

Draper et al. (2011) noted the evolution of the ratio of the polarization across the Balmer jump versus the V-band polarization occasionally traced out distinctive loops in PCD diagrams. Haubois et al. (2013) explored these diagrams in detail with theoretical models. Since the polarization change across the Balmer jump is roughly proportional to the density squared whereas the V-band polarization is proportional to the density, PCD diagrams offer a useful method to investigate the evolution of Be disks when spectral type and inclination can be constrained (Haubois et al. 2013). PCD loops observed in 60 Cyg and π Aqr were qualitatively modeled using the radiative transfer code HDUST and 1D hydrodynamical code SINGLEBE by turning the mass decretion rate on and off. Subsequent detailed modeling of PCDs demonstrated that the shape, slope, and time-scale of loops depends on spectral type, inclination angle, the base density of the disk, and the temporal behavior of the mass decretion rate (Haubois et al. 2013). One important conclusion from these modeling efforts is that steady state disks pause at the top of a PCD loop, while the disk is fed by either constant mass-loss or semi-regular mass injections from the star (Haubois et al. 2013). Our steady disk sample broadly reproduces this behavior. For example, both ϕ Per and γ Cas (Fig 2) cluster at high V-band polarization and high Balmer jump ratios in their PCDs during their steady-state disk stage.

However, the following systems have deviations from this steady state disk behavior:

4.2.1. 48 Lib

48 Lib exhibits clear evidence of a partial PCD loop (Fig 2a) in our dataset. The rise in 48 Lib’s intrinsic V-band polarization (blue points; Fig 2a) indicates a disk growth phase, which eventually plateaus into a steady state disk phase. Unlike other steady state disks in our sample that sit at the top of the PCD loop during the steady state, 48 Lib’s Balmer jump ratio rapidly drops during this phase. Since 48 Lib is a near edge-on inclination (Rivinius, Stefl, & Baade 2006; Stefl et al. 2012), its PCD behavior seems consistent with the modeling scenario outlined in Fig. 9 of Haubois et al. (2013). Specifically, these results suggest that 48 Lib was characterized by a high base density ($\approx 10^{-11}$ g cm $^{-3}$) disk and disk orientation which gives a high opacity. This manifests during the onset of the disk-growth event with a large Balmer jump ratio which later decreases at a nearly constant V-band polarization as it approaches a steady state phase. Furthermore, it has a steeper decline which is consistent with a later spectral type of B2 to B5 given 48 Lib is B3.

4.2.2. ψ Per

ψ Per experienced a notable rise in intrinsic V-band polarization during the early 1990’s (blue points; Fig 2b) indicating a disk growth phase, that seemingly plateaued during the later part of the decade into a stable phase. ψ Per exhibited a dramatic drop in its Balmer jump polarization as it transitioned to a steady state system. Given the mid spectral type (B5) and near edge-on inclination ($\sim 75^\circ$; Table 1) of the system, like 48 Lib, we suggest that the ψ Per PCD behavior could be caused by the outer regions of the high inclination, high density disk absorbing significant Balmer jump photons at the onset of the disk growth event (Haubois et al. 2013). This is further supported by the fact the polarization blueward of the Balmer jump was nearly zero, or essentially optically thick, to polarization of the disk.

4.2.3. 28 Cyg

During 28 Cyg’s overall long-term decline in disk strength, as measured by its declining intrinsic V-band polarization and H α EW (Fig. 2c), the system experienced three short, large jumps in Balmer jump polarization. During a 90 day period when the star was monitored regularly, in some cases nightly, the PCD diagram illustrates 3 instances where the Balmer jump ratio spiked to >2.5 (compared to the median value of 1.4). The separation between these three peaks was 24 and 18 days respectively. Given its spectral type (B2.5), the Balmer jump polarization is most sensitive to the inner regions of the disk when compared to the V-band polarization (Haubois et al. 2013). These Balmer jump ratio spikes (that occur at a constant V-band polarization) are likely caused by discrete events in the inner disk. Specifically, we speculate that the spikes stem from stochastic mass injections into the disk.

Although outside the scope of this paper, it is clear that detailed modeling of 48 Lib, ψ Per, and 28 Cyg

using codes such as Halonen & Jones (2013a) and Haubois et al. (2013) should be improved and pursued to reproduce the PCD variability observed in these systems. Moreover, given the diagnostic potential for systems experiencing full disk growth/disk-loss episodes (π Aqr, 60 Cyg; Draper et al. 2011) and episodic disk growth (48 Lib, ψ Per, 28 Cyg), it is certainly clear that enhanced observational monitoring of these types of systems should be aggressively pursued. Without consistent temporal monitoring, it can become challenging to constrain the exact time-scale for disk growth and loss events. Our results for 28 Cyg provide quantitative evidence that even high cadence (i.e. nightly) observations yield interesting PCD phenomenon that could be better exploited to diagnose episodic mass injection events.

4.3. One-armed Density Waves

Halonen & Jones (2013b) presented ad hoc model predictions of the effects of global one-armed oscillations (Okazaki 1991, 1997) on the time-dependent linear polarization of Be disks, including models that used a perturbation pattern characterized by a pattern of opposite overdense and underdense regions (Okazaki 1997) and models that used a spiral shaped perturbation pattern as adopted by Carciofi et al. (2009). These models (and those of Carciofi et al. 2009) predict that the V -band polarization and polarization across the Balmer jump should exhibit a clear inclination-dependent modulation with phase (Figs 6-8 of Halonen & Jones 2013b), although they will be out of phase with one another due to the different radial locations in the disks over which the scattering events occur in each bandpass. The V -band polarization position angle is also predicted to exhibit complex changes with phase (Fig 10; Halonen & Jones 2013b). In spite of these predictions, no conclusive observational evidence of this phenomenon has been reported (Carciofi et al. 2009).

γ Cas is known to exhibit V/R variations indicating the presence of a one-armed density feature in its disk, as seen in its phase-folded He I V/R ratios (Fig 3) compiled from data presented in Miroshnichenko et al. (2002). Observations were made at the Ritter observatory from 1993 to 2002 of the He I at 5876 Å, amongst other lines, with a resolving power of ~ 26000 . The line profile was consistently double peaked and had clear V/R variations γ Cas exhibits a generally stable disk, as diagnosed by its intrinsic polarization (Fig. 2a), which indicates its inner disk is being supplied by a generally stable decretion rate. It therefore makes an ideal system to search for long-term polarimetric effects related to its one-armed density feature. The intrinsic V -band polarization, polarization across the Balmer jump, and V -band polarization position angle phased to the V/R period of the He I data is shown in Fig 3. The intrinsic V -band polarization generally exhibits a double-oscillation pattern over one period that is predicted by Halonen & Jones (2013b). The intrinsic polarization across the Balmer jump exhibits variability, albeit no clear indication of the phase-lagged behavior predicted by Halonen & Jones (2013b). The intrinsic V -band polarization position angle suggestively exhibits evidence of cohesive variations as a function of phase, but such variations are an order

of magnitude greater than that predicted in the ad hoc models of Halonen & Jones (2013b). We speculate that one reason these data exhibit a stronger indication of the predicted behavior in V -band, rather in the Balmer jump polarization, is that the former is less sensitive to small changes in the inner disk caused by changes in the mass decretion rate. We encourage future modeling efforts of this phenomenon to explore the ramifications of abrupt and gradual changes in the mass decretion rate have on the polarization in disks having one-armed density waves.

4.4. PA Deviations

Wisniewski et al. (2010) reported numerous instances of the intrinsic polarization of 60 Cyg and π Aqr deviating from their linear trends on a Stokes QU diagram, and found that these deviations in intrinsic polarization position angle were more prominent during large outburst events. These authors interpreted this behavior as either evidence of the injection and subsequent circularization of new blobs of mass into the inner disk region, similar to that noted in Carciofi et al. (2007), or as evidence of the injection and subsequent circularization of new blobs at an inclined orbit to the plane of pre-existing disk material. Many of the Be systems explored in our current study exhibit generally stable, strong disks over most of the duration of our dataset, which suggests we should see analogous evidence of PA deviations in our dataset. As seen in Fig. 4, γ Cas exhibits PA deviance as a function of the intrinsic V -band polarization in the system. Analogous figures for our other targets are available in the online-version of this paper. Overall, we do see clear evidence of strong PA deviations in most of our Be stars even though they cannot be correlated to specific outburst events like 60 Cyg and π Aqr were. The system that exhibits the smallest level of PA deviations, ω Ori, is noteworthy as it exhibited evidence of a gradual, albeit incomplete, loss of its disk throughout the time-frame covered by our data. While errors in the ISP estimate could be inducing errors in the intrinsic PA, we note that the deviations are symmetric about the mean. If there were errors in our PA determinations, then one would expect the deviations to be systematically offset to one side of the mean. If there were a PA estimate error then one would expect the deviations systematically offset to one side of the mean. In general, our results are consistent with systems which have had more precise ISP determinations and time resolved outbursts which suggest the PA deviations are also “clumpy” injection events (e.g. 60 Cyg and π Aqr).

4.5. Be+sdO systems

Three of our targets are known to have a sub dwarf companion, ϕ Per (Gies et al. 1998), FY CMA (Peters et al. 2008), and 59 Cyg (Peters et al. 2013), and all three systems exhibit steady state disks in our data. This apparent stability could be influenced by the sdO truncating these disks to the maximum allowed radius. Interestingly, we do observe significant variability in the polarization across the Balmer jump in both FY CMA and 59 Cyg (Fig 2c). We remind the reader that the ISP for 59 Cyg was poorly constrained; however, we explored different assumed total ISP PA values (about PA = 0) and still observed the jumps in the polarization across the Balmer jump, suggesting that they are likely real.

As the sdO is likely heating the outer region of the disk nearest its orbital position, we speculate that this outside heating source may inflate the scale height of this region of the disk. Given the short periods of order 29-37 days (Peters et al. 2013), we speculate that when the inflated scale heights of these moderately high inclination disks (Table 1) pass in front of our line of sight with the star, they cause the observed changes in polarization across the Balmer jump. We further speculate that the amount of disk material heated and inflated by ϕ Per’s more distant (127 day period) sdO companion may contribute to why this system exhibits no analogous Balmer jump polarization jumps. Higher cadence observations that sufficiently sample the suggested puffed-up outer disk over the orbital period of these systems’ sdO companion would help to further establish our interpretation of this observational phenomenon.

4.6. Maximum Polarization

The maximum polarization for a viscous disk in equilibrium is found to be correlated with inclination, spectral type, and base density (Haubois et al. 2013; Halonen & Jones 2013b). In most cases the disks in this sample reach some form of steady state. We then assume that the maximum observed polarization at some point in the 15 year survey is the maximum polarization of a disk around these stars. Since the effective temperature and inclination can be determined by other means (e.g. spectroscopy and interferometry), we use literature values to then derive the range of base densities for this sample of Be stars (See Table 1). Given the model tracks of Haubois et al. (2013), we find that the base density for these stars lie within 8×10^{-11} to $4 \times 10^{-12} \text{ g cm}^{-3}$ (See Fig.5).

Several items are key to interpreting the base density estimates extracted from Figure 5. π Aqr, for example, exhibits a lower maximum V-band polarization than the $4.2 \times 10^{-11} \text{ g cm}^{-3}$ base density track compared to other stars having a similar stellar effective temperature (Figure 5; right panel) due in part because the system’s inclination angle (33.6°) is lower than that used for the model track (70°). Similarly, π Aqr exhibits a higher maximum than expected for the $4.2 \times 10^{-11} \text{ g cm}^{-3}$ base density track (Figure 5; left panel) compared to other systems having a similar inclination due in part to π Aqr having a warmer stellar effective temperature than adopted for these models. Due to this degeneracy, it likely has a similarly large base density as ϕ Per around $4.2 \times 10^{-11} \text{ g cm}^{-3}$. ψ Per and 59 Cyg have similar maximum polarization and inclination yet have very different effective temperatures. This then requires a low base density of $8.4 \times 10^{-12} \text{ g cm}^{-3}$ which exhibits maximum polarization independent of effective temperature. An object like γ Cas, shows behavior similar to that of π Aqr in relation to the model tracks. It is likely limited in maximum polarization due to its low inclination rather than its spectral type, so it is consistent with a low base density of $4.2 \times 10^{-11} \text{ g cm}^{-3}$. Due to the degeneracy and variable nature of some of the stars observed by HPOL, these limits are not meant to be absolute but rather a first look into the disk properties for the class as a whole. Each star will require more detailed modeling, but potentially broader statistics could be applied to a wider sample if polarimetry, spectroscopy, and interferometry can be obtained simultaneously to derive

the applicable parameters.

5. SUMMARY

Motivated by the recent discovery of the diagnostic power of polarization color diagrams (PCD) in characterizing the time-dependent mass decretion rate in Be stars (Draper et al. 2011), and the recent theoretical explorations and predictions of the utility of this diagnostic (Halonen & Jones 2013a,b; Haubois et al. 2013), we carefully analyzed the long-term polarimetric behavior of 9 additional classical Be stars. Our targets included systems exhibiting evidence of partial disk-loss/disk-growth episodes as well as systems exhibiting long-term stable disks. After characterizing and removing the ISP along the line of sight to each of these targets, we found:

1. Our steady-state Be disk sample (e.g. ϕ Per and γ Cas (Fig 2a) tend to simultaneously exhibit high intrinsic V-band polarization and high Balmer jump ratios in their PCDs, which confirms the behavior predicted by theory (Halonen & Jones 2013a; Haubois et al. 2013).
2. The PCDs for several later spectral type, highly inclined Be stars in our sample (e.g. 48 Lib and ψ Per, Fig 2) exhibit rapid declines in their Balmer jump ratios at epochs of continuously high intrinsic V-band polarizations, which provides the first observational confirmation of this predicted (Haubois et al. 2013) behavior. As noted by Haubois et al. (2013), this phenomenon can be produced when the base density of the disk is very high, and the outer region of the edge-on disk starts to self absorb a significant number of Balmer jump photons.
3. We observe numerous, brief jumps in the intrinsic polarization across the Balmer jump in 28 Cyg, ϕ Per, FY CMA, and 59 Cyg. The high cadence of our 28 Cyg data suggest these jumps are likely caused by stochastic injections of material into the inner disk (of this system). ϕ Per, FY CMA, and 59 Cyg are known sdO systems. We speculate that the sdO companion in these systems might be thermally inflating the outer region of one side of these disks, and that the observed Balmer jump polarization changes might be related to this inflated disk region passing in front of our line of sight as an alternative to blob injection events. We recommend future high cadence observations of these systems over the orbital periods of their sdO companions be obtained to confirm our interpretation.
4. We observe suggestive evidence of coherent variability in the intrinsic V-band polarization and polarization position angle of γ Cas that phases with the orbital period of a known one-armed density structure in this disk, similar to the theoretical predictions of Halonen & Jones (2013b). We speculate that the “astrophysical noise”

present in these trends, and our non-detection of the predicted (Halonen & Jones 2013b) phased trend in the polarization across the Balmer jump, could be caused by stochastic changes in the mass decretion rate in this system.

5. We also provide constraints on the base densities of quasi-static disks given our sample. Given the degeneracy between inclination and spectral type with the max polarization, we can only estimate the base densities are within $\approx 8 \times 10^{-11}$ to $\approx 4 \times 10^{-12} \text{ g cm}^{-3}$.

6. ACKNOWLEDGMENTS

We would like to thank the referee, Carol Jones, for helpful comments which improved this paper. We thank Brian Babler for his invaluable assistance with various aspects of HPOL data, and the HPOL and Ritter science teams for support of data acquisition. We also thank Kenneth H. Nordsieck for providing access

to the HPOL spectropolarimeter, and Anatoly Miroshnichenko for supplying an electronic copy of his archival γ Cas data. ZHD acknowledges partial support from the University of Washington Pre-MAP program, NSF REU at the University of Toledo, and the Washington Space Grant/NASA Summer Undergraduate Research Program. HPOL and WUPPE observations were supported under NASA contract NAS5-26777 with the University of Wisconsin-Madison. XH wants to thank FAPESP for the grant 2009/07477-1. ACC acknowledges support from CNPQ (grant 307076/2012-1) and FAPESP (grant 2010/19029-0). Observations at the Ritter Observatory are supported by the NSF under the PREST grant AST 04-40784. This study has made use of the SIMBAD database, operated at CDS, Strasbourg, France, the NASA ADS service, and the STScI MAST Archive. We also like to thank the Astronauts and Space Shuttle support crews for the successful completion of STS-35 and STS-67 which obtained data presented in this paper.

REFERENCES

- Bjorkman, J. E., & Cassinelli, J. P. 1993, *ApJ*, 409, 429
 Bjorkman, J.E. & Carciofi, A.C. 2005, in *The Nature and Evolution of Disks Around Hot Stars* (ASP Conf Ser. 337), ed. R. Ignace & K. Gayley (San Francisco, CA: ASP), 75
 Brown, J.C., Cassinelli, J.C., & Maheswaran, M. 2008, *ApJ*, 688, 1320
 Cantanzaro, G. 2013, *A&A*, 550, 79
 Carciofi, A.C., Magalhaes, A.M., Leister, N.V., Bjorkman, J.E., & Levenhagen, R.S. 2007, *ApJL*, 671, 49
 Carciofi, A.C., Okazaki, A.T., le Bouquin, J.-B., Stefl, S., Rivinius, Th., Baade, D., Bjorkman, J., & Hummel, C.A. 2009, *A&A*, 504, 915
 Carciofi, A.C. 2011, in *Active OB Stars: Structure, Evolution, Mass Loss and Critical Limits* (IAU Symp. 272), ed. C. Neiner et al. (Cambridge: Cambridge Univ. Press), 325
 Carciofi, A.C.; Bjorkman, J.E.; Otero, S.A.; Okazaki, A.T.; tefl, S.; Rivinius, T.; Baade, D.; Haubois, X., 2012, *ApJ*, 744, 15
 Cassinelli, J.P., Brown, J.C., Maheswaran, M., Miller, N.A., & Telfer, D.C. 2002, *ApJ*, 578, 951
 Clark, J.S., Tarasov, A.E., & Panko, E.A. 2003, *A&A*, 403, 239
 Clarke, D. & Bjorkman, K.S. 1998, *A&A*, 331, 1059
 Clayton, G.C. et al. *AJ*, 114, 1132
 Coyne, G.V. & Kruszewski, A. 1969, *AJ*, 74, 528
 Cranmer, S.R. 2005, *ApJ*, 634, 585
 Cranmer, S.R. 2009, *ApJ*, 701, 396
 Delaa, O. et al. 2011, *A&A*, 529, 87
 Doazan, V., Franco, M., Rusconi, L., Sedmak, G., & Stalio, R. 1983, *A&A*, 128, 171
 Draper, Z.H., Wisniewski, J.P., Bjorkman, K.S., Haubois, X., Carciofi, A.C., Bjorkman, J.E., Meade, M.R., & Okazaki, A. 2011, *ApJL*, 728, 40
 Frémat, Y.; Zorec, J.; Hubert, A.-M.; Floquet, M., 2005, *A&A*, 440, 305
 Gies, D. R., Bagnuolo, W. G., Jr., Ferrara, E. C., et al. 1998, *ApJ*, 493, 44
 Halonen, R.J., Mackay, F.E., & Jones, C.E. 2013, *ApJS*, 204, 11
 Halonen, R.J. & Jones, C.E. 2013, *ApJ*, 765, 17
 Halonen, R.J. & Jones, C.E. 2013, *ApJ*, in press
 Harries, T.J., Babler, B.L., & Fox, G.K. 2000, *A&A*, 361, 273
 Haubois, X., Carciofi, A.C., Rivinius, Th., Okazaki, A.T., & Bjorkman, J.E. 2012, *ApJ*, 756, 156
 Haubois, X., Mota, B. C., Carciofi, A. C., Draper, Z. H., Wisniewski, J. P., Bednarski, D. & Rivinius, Th., 2013, *ApJ*, submitted
 Heiles, C. 2000, *AJ*, 119, 923
 Hummel, W. & Vrancken, M. 2000, *A&A*, 359, 1075
 Kraus, S. et al. 2012, *ApJ*, 744, 19
 Koubský, S. et al. 2000, *A&A*, 356, 913
 Lee, U., Osaki, Y., & Saio, H. 1991, *MNRAS*, 250, 432
 Mathewson, D.S. & Ford, V.L. 1970, *MmRAS*, 74, 139
 McLean, I. S., & Brown, J. C. 1978, *A&A*, 69, 291
 McSwain, M.V., Huang, W., Gies, D.R., Grundstrom, E.D., & Townsend, R.H.D. 2008, *ApJ*, 672, 590
 McSwain, M.V., Huang, W., & Gies, D.R. 2009, *ApJ*, 700, 1216
 Meilland, A. et al. 2007, *A&A*, 464, 59
 Meilland, A. et al. 2007, *A&A*, 464, 73
 Miroshnichenko, A.S. et al. 2001, *A&A*, 377, 485
 Miroshnichenko, A. S., Bjorkman, K.S., & Krugov, V.D. 2002, *PASP*, 14, 1226
 Miroshnichenko, A.S. et al. 2003, *A&A*, 408, 305
 Miroshnichenko, A.S. et al. 2013, *ApJ*, 766, 119
 Neiner, C. et al. 2002, *A&A*, 388, 899
 Nook, M. 1990, Ph.D. dissertation, The University of Wisconsin-Madison
 Nordsieck, K. H., & Harris, W. 1996, *ASP Conf. Ser.* 97, *Polarimetry of the Interstellar Medium*, ed. W. G. Roberge & D. C. B. Whittet (San Francisco: ASP), 100
 Nordseick, K.H., Code, A.D., Anderson, C.M., Meade, M.R., Babler, B., Michalski, D.E., Pfeifer, R.H., Jones, T.E. 1994, *SPIE*, 2010, 2
 Okazaki, A.T. 1991, *PASJ*, 43, 75
 Okazaki, A.T. 1997, *A&A*, 318, 548
 Perryman, M.A. et al. 1997, *A&A*, 323, 49
 Peters, G. J., Gies, D. R., Grundstrom, E. D., & McSwain, M. V. 2008, *ApJ*, 686, 1280
 Peters G.J., Pewett T.D., Gies D.R., Touhami Y.N., and Grundstrom E.D. 2013, *ApJ*, 765, 2
 Poeckert, R., Bastien, P., & Landstreet, J. D. 1979, *AJ*, 84, 812
 Porter, J.M. & Rivinius, T. 2003, *PASP*, 115, 1153
 Pott, J.-U. et al. 2010, *ApJ*, 721, 802
 Quirrenbach, A., Bjorkman, K. S., Bjorkman, J. E., Hummel, C. A., Buscher, D. F., Armstrong, J. T., Mozurkewich, D., Elias, N. M., & Babler, B. L. 1997, *ApJ*, 479, 477
 Rivinius, Th., Baade, D., Stefl, S., Stahl, O., Wolf, B., & Kaufer, A. 1998, *A&A*, 333, 125
 Th. Rivinius, A.C. Carciofi, & C. Martayan, 2013, *A&AR*, accepted.
 Rivinius, Th., Stefl, S., & Baade, D. 2006, *A&A*, 459, 137
 Serkowski, K., Mathewson, D. S., & Ford, V. L. 1975, *ApJ*, 196, 261
 Stee, P. 2011, in *Active OB Stars: Structure, Evolution, Mass Loss and Critical Limits* (IAU Symp. 272), ed. C. Neiner et al. (Cambridge: Cambridge Univ. Press) 313
 Stefl, S., Le Bouquin, J.-B., Carciofi, A.C., Rivinius, Th., Baade, D., & Rantakyro, F. 2012, *A&A*, 540, 76
 Touhami, Y.; Gies, D. R.; Schaefer, G. H.; McAlister, H. A.; Ridgway, S. T.; Richardson, N. D.; Matson, R.; Grundstrom, E. D.; ten Brummelaar, T. A.; Goldfinger, P. J.; Sturmann, L.; Sturmann, J.; Turner, N. H.; Farrington, C., 2013, *ApJ*, 768, 128
 Townsend, R.H.D., Owocki, S.P., & Howarth, I.D. 2004, *MNRAS*, 350, 189
 Underhill, A. & Doazan, V. eds. 1982, *B Stars with and without Emission Lines* (NASA SP-456; Washington DC: NASA)
 Vinicius, M.M.F., Zorec, J., Leister, N.V., & Levenhagen, R.S. 2006, *A&A*, 446, 643
 Wheelwright, H. E., Bjorkman, J. E., Oudmaijer, R. D., et al. 2012, *MNRAS*, 423, L11
 Wilking, B. A., Lebofsky, M. J., & Rieke, G. H. 1982, *AJ*, 87, 695

- Wisniewski, J.P., Kowalski, A.F., Bjorkman, K.S., Bjorkman, J.E., & Carciofi, A.C. 2007a, *ApJL*, 656, 21
- Wisniewski, J.P., Bjorkman, K.S., Magalhaes, A.M., Bjorkman, J.E., Meade, M.R., & Pereyra, A. 2007b, *ApJ*, 671, 2040
- Wisniewski, J.P., Draper, Z.H., Bjorkman, K.S., Meade, M.R., Bjorkman, J.E., & Kowalski, A.F. 2010, *ApJ*, 709, 1306
- Wolff, M. J., Nordsieck, K. H., & Nook, M. A. 1996, *AJ*, 111, 856
- Wood, K. & Bjorkman, J.E. 1995, *ApJ*, 443, 348
- Wood, K., Bjorkman, J. E., Whitney, B. A., & Code, A. D. 1996a, *ApJ*, 461, 828
- Wood, K., Bjorkman, J. E., Whitney, B. A., & Code, A. D. 1996b, *ApJ*, 461, 847
- Wood, K., Bjorkman, K. S., & Bjorkman, J. E. 1997, *ApJ*, 477, 926

TABLE 1
TARGET STAR SUMMARY

Star	Spectral Type	T_{eff}	Inclination	# of HPOL Reticon nights	# of HPOL CCD nights	WUPPE
48 Libra	B3Ve	17645±554 ¹	~90 ^{7,8}	13	7	Astro-2
ψ Persei	B5Ve	15767±509 ¹	75±8 ⁴ ; 75 ⁶	9	10	Astro-2
ϕ Persei	B2Vpe	25556±659 ¹	84 ⁵ ; 72 ⁶	15	11	Astro-2
28 Cygni	B2.5Ve	18353±516 ¹	64 ⁶	4	31	N/A
66 Ophiuchi	B2Ve	21609±523 ¹	48 ⁶	7	3	N/A
γ Cassiopeia	B0.5IVpe	26431±618 ¹	44 ⁵ ; 76 ⁶	9	14	N/A
ω Orionis	B3IIIe	20200 ²	N/A	10	8	N/A
FY Canis Majoris	B1II	21750±655 ¹	55 ⁶	9	14	N/A
59 Cygni	B1.5Vnne	21750±655 ¹	72 ⁵ 73 ⁶	10	8	Astro-2
60 Cygni	B1Ve	27000 ³	N/A	2	27	N/A
π Aquarii	B1Ve	26061±736 ¹	33.6 ⁶	53	57	Astro-1

NOTE. — A summary of the spectropolarimetric data analyzed in this paper. Spectral types were adopted from SIMBAD, except for 48 Lib which is identified as B3 in a more detailed study (Steff et al. 2012). Sources for the effective temperature include ¹Frémat et al. (2005), ²Cantanzaro (2013), and ³Koubský et al. (2000). Sources for the disk inclinations include ⁴Delaa et al. (2011), ⁵Touhami et al. (2013), ⁶Frémat et al. (2005), ⁷Rivinius, Steff, & Baade (2006), ⁸Steff et al. (2012). The number of observations used for each star during the survey is listed by which detector was used. If the target was observed with the Wisconsin Ultraviolet Photo-Polarimeter Experiment (WUPPE), the mission which took the data is listed.

TABLE 2
RAW HPOL DATA

Target Name	Julian Date	%Q (V-band)	%U (V-band)	%Err	H α EW
48 Lib	2447679.2	-0.614	-0.497	0.005	-21.5
48 Lib	2448003.2	-0.544	-0.591	0.003	-19.7
48 Lib	2448012.2	-0.575	-0.530	0.006	-20.0

NOTE. — The raw V-band polarization and H α equivalent width is presented for every observation of all of our target stars. The full version of this table is available in the online version from this journal.

TABLE 3
FIELD STAR POLARIZATION DATA

Target Star	Field Star	Spectral Type	Distance(pc)	%Pol.	% Error	P.A.	P.A. error
48 Lib	HD145748	K5III	275.4	0.420	0.035	99.6	2.4
...	HD144639	F3IV	144.5	1.060	0.048	86.7	1.3
...	HD145153	K0III	120.0	0.760	0.036	86.3	1.4
...	HD145897	K3III	104.7	0.310	0.035	111.8	3.2
...	AVG	92.93	10.73
ϕ Per
ψ Per	HD23049	K4III	125.9	0.500	0.032	113	1.8
...	HD21278	B5V	150.0	0.480	0.120	120	7.1
...	HD20902	F5Iab	162.0	0.410	0.120	100	8.3
...	HD21428	B3V	168.0	0.287	0.141	127.2	13.8
...	HD20809	B5V	169.0	0.569	0.102	104	5.1
...	AVG	112	11.1
π Aqr	HD213119	K5III	132	0.23	0.035	110.4	4.4
...	HD212320	G6III	87	0.39	0.017	160.0	1.2
...	HD211924	B5III	251	1.17	0.037	140.3	0.9
...	HD211838	B8V	120	0.46	0.035	138.8	2.2
...	HD211304	B9	306	0.22	0.035	107.6	4.5
...	HD211099	B6	417	0.26	0.038	119.2	4.2
...	AVG	109.22	1.61
60 Cyg	HD198915	B6V	475	0.19	0.120	15.0	17.5
ω Ori	HD36267	B5V	143	0.133	0.026	164.7	5.6
...	HD37606	B8V	242	0.150	0.032	36.0	6.1
...	HD38650	B9	352	0.134	0.023	42.0	4.9
...	HD38900	B9	360	0.074	0.026	20.0	10.0
...	AVG	36	9.7
28 Cyg	HD192383	G5III	109	0.190	0.030	131.2	4.5
...	HD192934	A0V	109	0.170	0.050	71.1	8.4
...	HD192182	G8III	113	0.080	0.030	77.3	10.6
...	HD189751	K1III	155	0.150	0.040	63.5	7.6
...	HD192124	A5III	156	0.070	0.030	61.6	12.1
...	HD191046	K0III	159	0.080	0.032	80	11.3
...	HD193636	A7III	197	0.060	0.060	3.4	26.6
...	HD191045	K5III	229	0.130	0.032	61.0	7.0
...	HD192745	A0V	254	0.120	0.050	86.0	11.8
...	HD194357	B9II	316	0.440	0.032	76.0	2.1
...	HD227421	A5III	347	0.260	0.080	94.7	8.7
...	AVG	79	35
66 Oph	HD162177	A0	288	0.600	0.060	77.7	2.9
...	HD162954	B7	288	0.740	0.035	75.7	1.4
...	HD163592	B8	288	0.820	0.042	92.8	1.5
...	HD162649	A0	302	0.960	0.073	79.5	2.2
...	HD164097	A0	302	0.670	0.066	68.8	2.8
...	HD162993	A0	331	0.630	0.073	73.4	3.3
...	HD163152	A0	347	0.600	0.073	75.3	3.5
...	HD163591	B8	347	1.030	0.055	85.8	1.5
...	AVG	81	8.5
FY CMa	HD56094	B2IV	1645	0.310	0.100	126.4	9.2
...	HD59612	A5I	686	0.460	0.035	159.1	2.2
...	HD61227	F0II	391	1.140	0.040	125.0	1.0
...	AVG	136	18
59 Cyg	HD202654	B2V	549	0.180	0.200	24.0	29.1
...	BD+44.3627	B3V	504	0.780	0.180	46.0	6.6
...	HD198915	B6V	475	0.190	0.120	15.0	17.5
...	HD201836	B5V	246	1.060	0.200	21.0	5.4
...	AVG	29	35

NOTE. — Archival *V*-band polarization data for field stars used in this manuscript, compiled from ¹Mathewson & Ford (1970) and ²Heiles (2000), are listed. Spectral types for the field stars were obtained from SIMBAD, and distance measurements were obtained from the Hipparcos catalog (Perryman et al. 1997).

TABLE 4
FINAL INTERSTELLAR POLARIZATION PARAMETERS

Star	%P	θ	λ_{max}	%P $_{\perp}$	%P $_{\parallel}$
48 Lib	0.86	93	5593	-0.78	-0.36
ϕ Per	0.76	99	4539	0.40	-0.65
γ Cas	0.31	95	3786	0.15	-0.27
66 Oph	0.45	81	5466	0.25	-0.37
ω Ori	0.23	110	4442	0.12	-0.19
ψ Per	0.09	112	528	0.065	-0.06
28 Cyg	0.25	79	5496	-0.22	-0.10
FY CMa	0.04	136	3545	-0.03	0.03
59 Cyg	0.51	0	5805	-0.18	0.47
60 Cyg	0.11	41.5	5349	0.08	0.07
π Aqr	0.50	108.7	5123	-0.45	-0.22

NOTE. — The final parameters for the parallel component (%P $_{\parallel}$), perpendicular component (%P $_{\perp}$), and net (%P) interstellar polarization for each of our target stars is compiled.

TABLE 5
INTRINSIC POLARIZATION

Target Name	Julian Date	%Q (V-band)	%U (V-band)	%Err
48 Lib	2447679.2	0.233	-0.410	0.005
48 Lib	2448003.2	0.304	-0.504	0.003
48 Lib	2448012.2	0.273	-0.442	0.006

NOTE. — The intrinsic V-band polarization is presented for every observation of all of our target stars. The full version of this table is available in the online version of this journal.

TABLE 6
66 OPH RITTER DATA

Julian Date	EW
2450930.9	-38.1
2450952.8	-36.4
2450999.7	-35.2
2451058.6	-34.7
2451777.6	-26.3
2451809.5	-25.2
2451814.5	-25.3
2451987.9	-23.9
2452033.8	-23.0
2452086.8	-22.1
2452105.7	-22.7
2452128.6	-22.3
2452164.5	-21.8
2452450.7	-20.5
2452461.8	-20.3
2452757.8	-15.4
2452792.8	-14.6
2452818.8	-14.2
2452849.6	-15.1
2452876.6	-14.8
2452898.6	-15.1
2453162.8	-12.4
2453187.7	-12.4
2453223.6	-12.3
2453259.6	-12.2
2453553.7	-10.9
2453623.6	-12.2
2453648.5	-11.5

NOTE. — Supplementary H α EW measurements from spectra of 66 Oph obtained at Ritter Observatory.

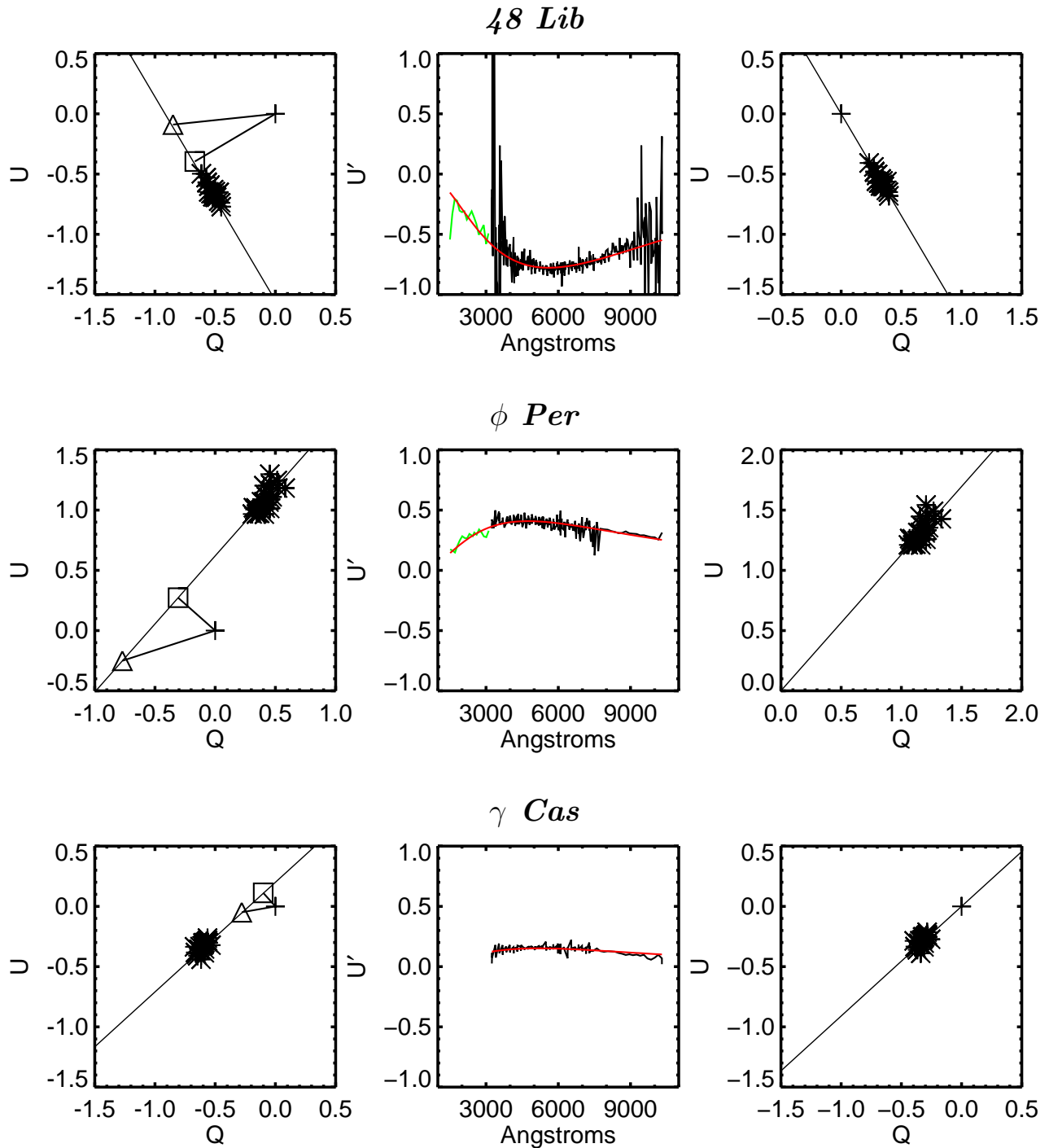


FIG. 1A.— The left panel depicts the raw V -band polarization for a target star plotted on a Stokes QU diagram along with the intrinsic disk position angle vector overlaid. Either the best fit linear regression or the multi-epoch polarization change across the Balmer jump was used to define the position angle of the disk major axis. The ISP_{\perp} (square) and ISP_{total} (triangle) vectors are also overlaid. The center panel depicts the wavelength dependence of the U' data (WUPPE data shown in green, HPOL data shown in black), formed by rotating the V -band polarization by the PA of the disk major axis. The best fit Serkowski law fit (red) parameterizes the ISP_{\perp} and $ISP_{\lambda_{max}}$ components (Table 4).

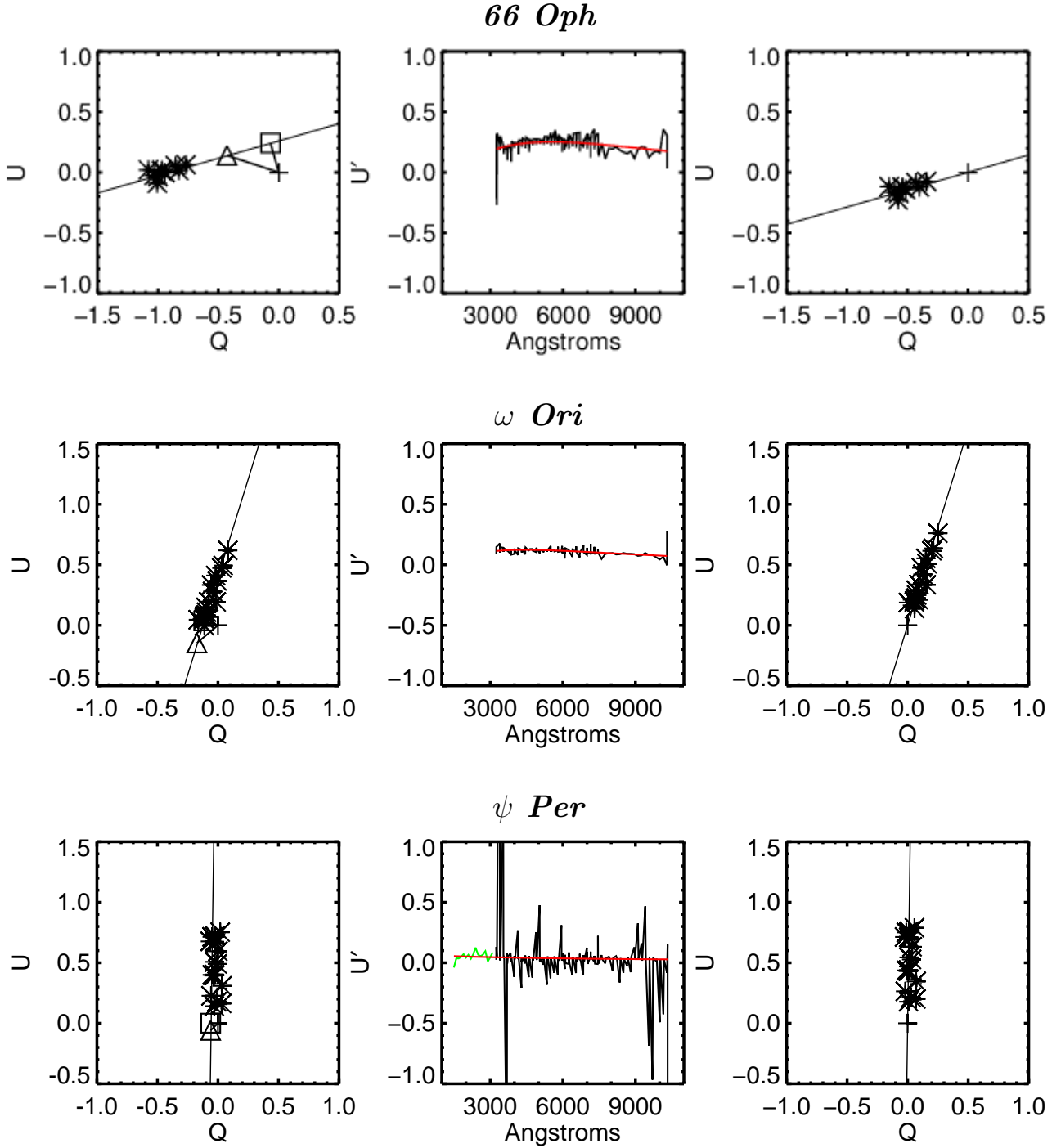


FIG. 1B.— The left panel depicts the raw V -band polarization for a target star plotted on a Stokes QU diagram along with the intrinsic disk position angle vector overlaid. Either the best fit linear regression or the multi-epoch polarization change across the Balmer jump was used to define the position angle of the disk major axis. The ISP_{\perp} (square) and ISP_{total} (triangle) vectors are also overlaid. The center panel depicts the wavelength dependence of the U' data (WUPPE data shown in green, HPOL data shown in black), formed by rotating the V -band polarization by the PA of the disk major axis. The best fit Serkowski law fit (red) parameterizes the ISP_{\perp} and $ISP_{\lambda_{max}}$ components (Table 4).

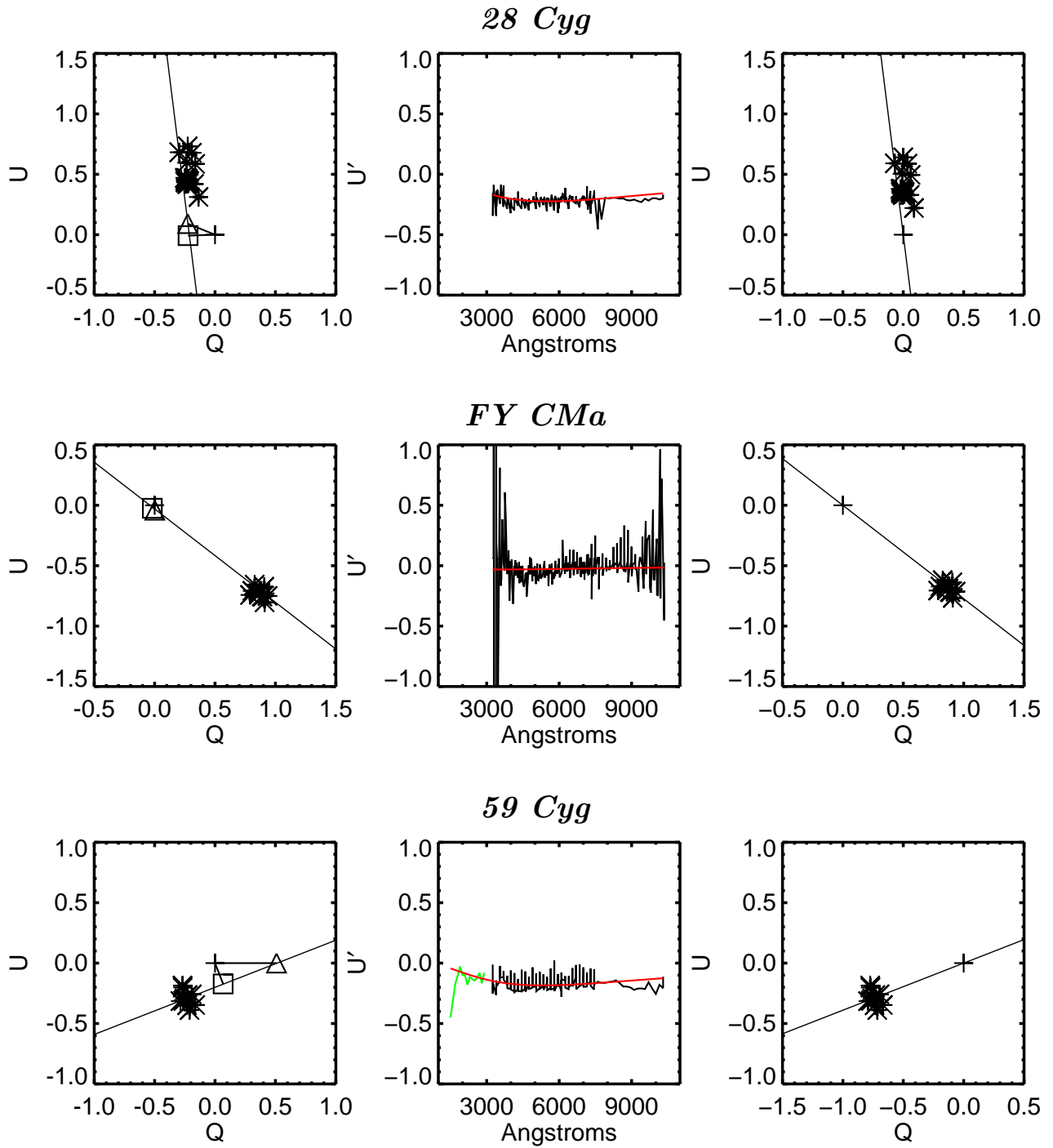


FIG. 1c.— The left panel depicts the raw V-band polarization for a target star plotted on a Stokes QU diagram along with the intrinsic disk position angle vector overlaid. Either the best fit linear regression or the multi-epoch polarization change across the Balmer jump was used to define the position angle of the disk major axis. The ISP_{\perp} (square) and ISP_{total} (triangle) vectors are also overlaid. The center panel depicts the wavelength dependence of the U' data (WUPPE data shown in green, HPOL data shown in black), formed by rotating the V-band polarization by the PA of the disk major axis. The best fit Serkowski law fit (red) parameterizes the ISP_{\perp} and $ISP_{\lambda_{max}}$ components (Table 4).

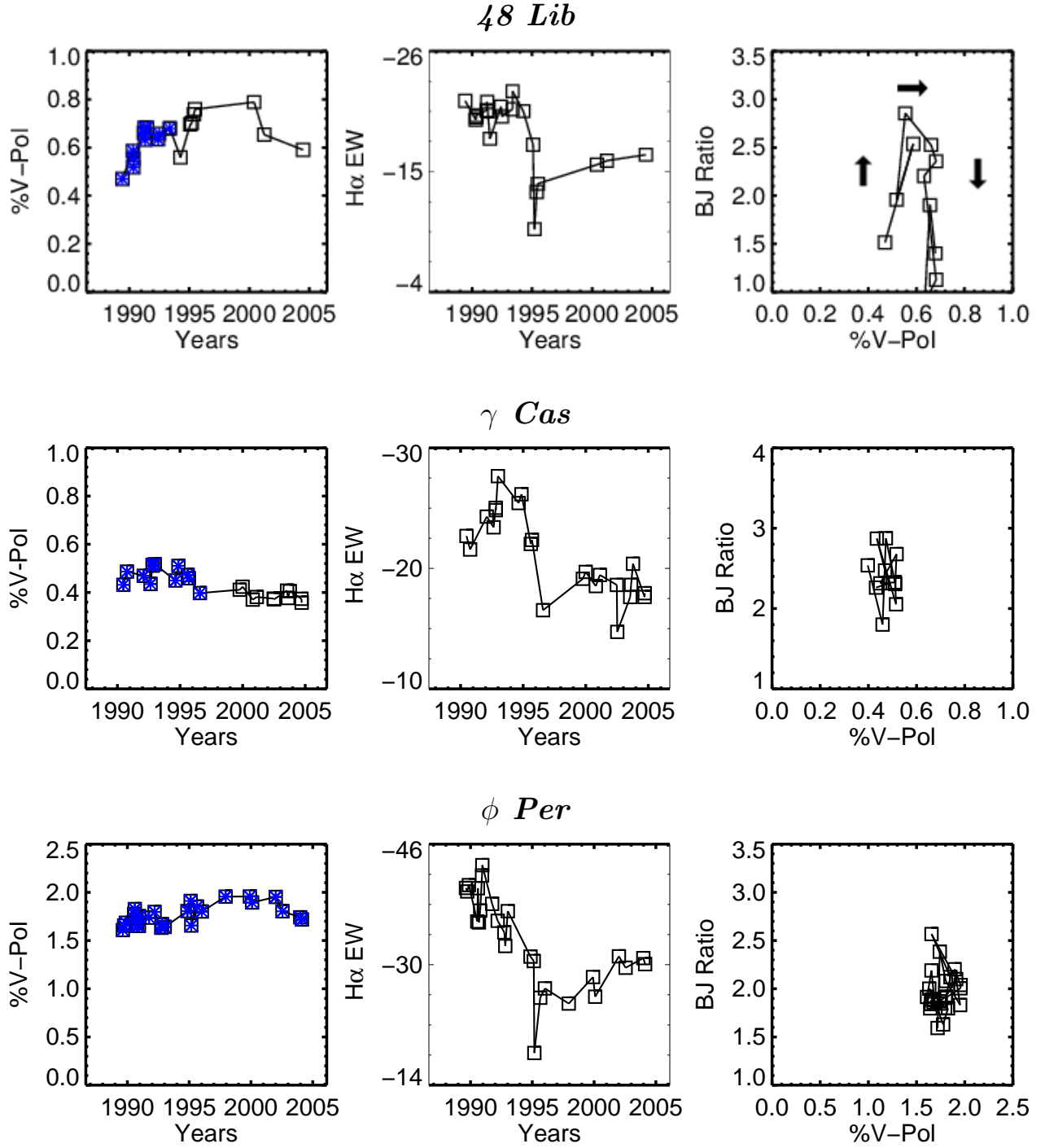


FIG. 2A.— The time evolution of the intrinsic V-band polarization of the target stars are in the left panel and the H α equivalent width (EW) are shown in the center panel. EWs measured by HPOL data are shown in squares while EWs measured from spectra obtained at Ritter Observatory are shown in triangles. The flux offset is due to HPOL not being flux calibrated. The right panel depicts the PCD for the portion of the V-band % Pol data cross-marked in blue on the left panel.

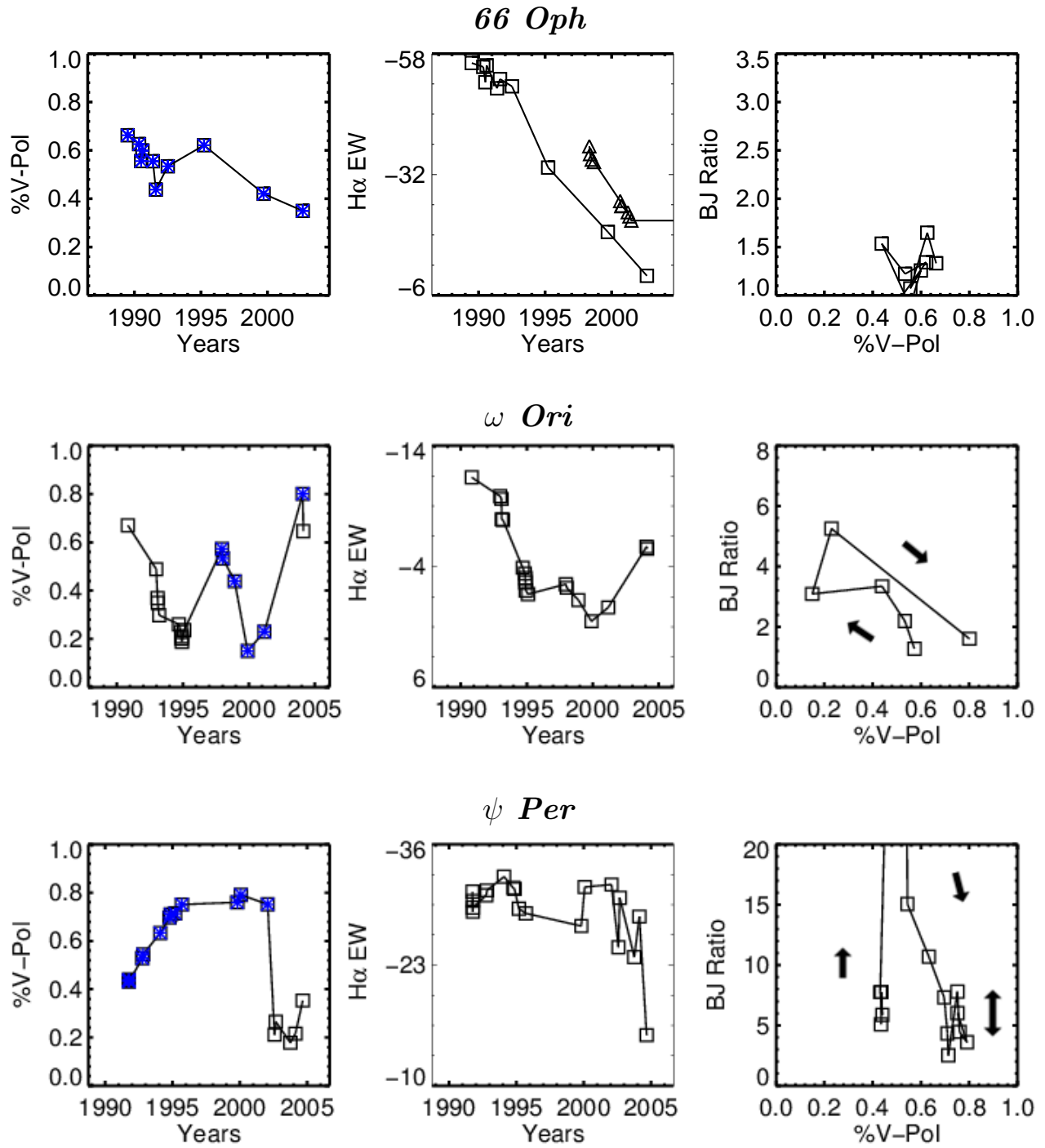


FIG. 2B.— The time evolution of the intrinsic V-band polarization of the target stars are in the left panel and the H α equivalent width (EW) are shown in the center panel. EWs measured by HPOL data are shown in squares while EWs measured from spectra obtained at Ritter Observatory are shown in triangles. The flux offset is due to HPOL not being flux calibrated. The right panel depicts the PCD for the portion of the V-band % Pol data cross-marked in blue on the left panel.

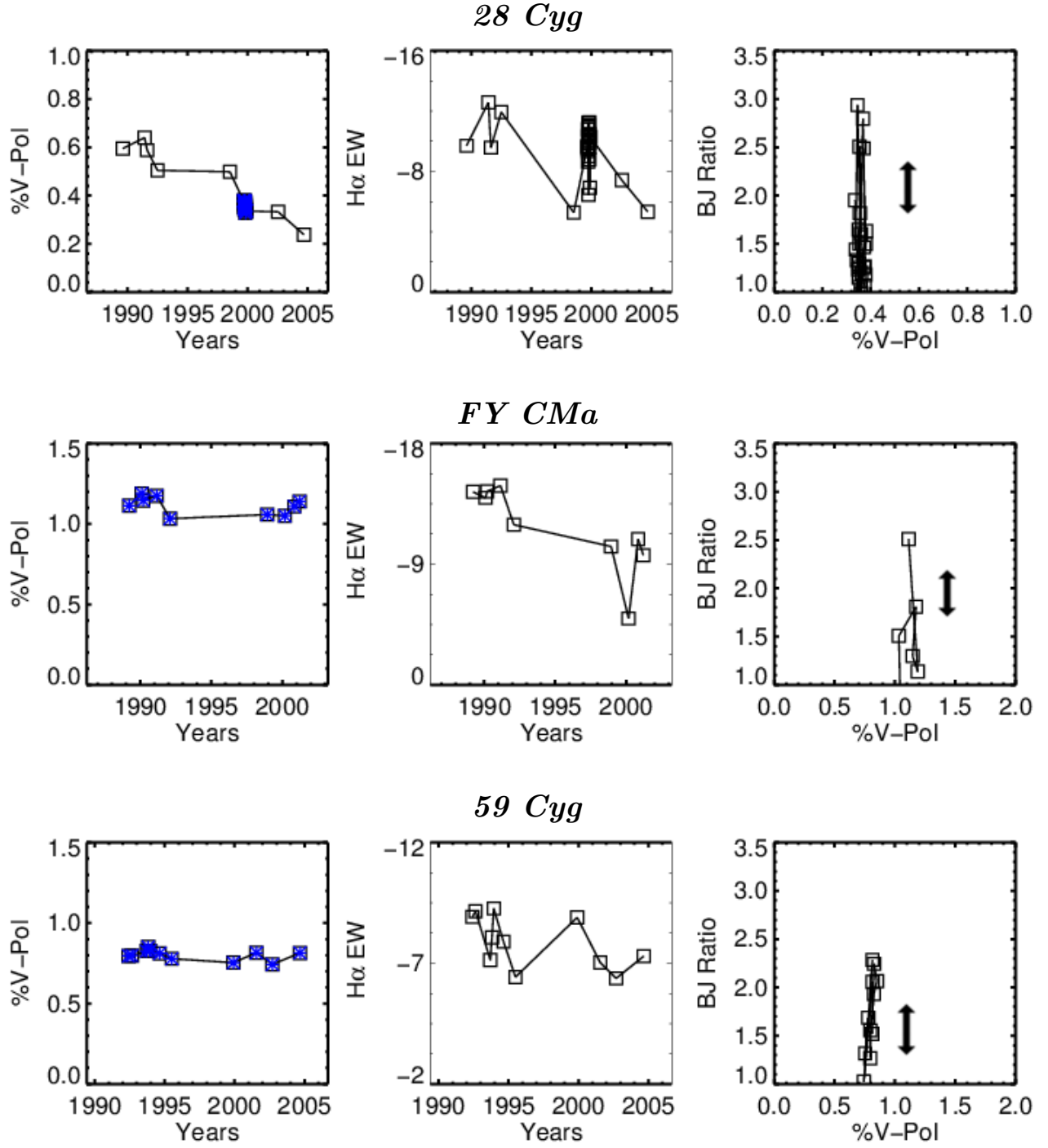


FIG. 2c.— The time evolution of the intrinsic V-band polarization of the target stars are in the left panel and the H α equivalent width (EW) are shown in the center panel. EWs measured by HPOL data are shown in squares while EWs measured from spectra obtained at Ritter Observatory are shown in triangles. The flux offset is due to HPOL not being flux calibrated. The right panel depicts the PCD for the portion of the V-band % Pol data cross-marked in blue on the left panel.

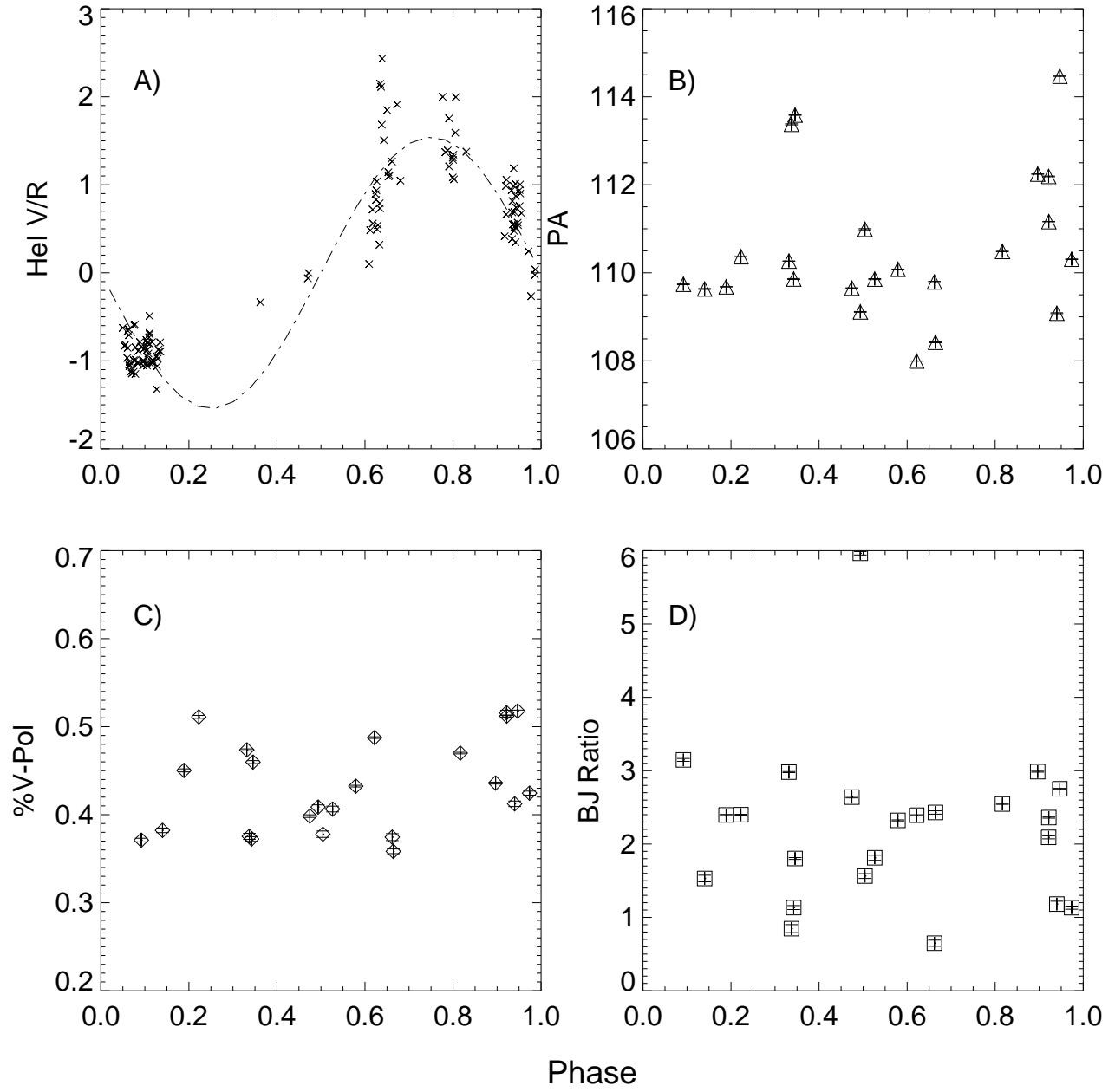


FIG. 3.— The phase folded He I V/R measurements (adopted from Miroshnichenko et al. 2002; panel A), the phase folded intrinsic V-band polarization position angle (panel B), the phase folded intrinsic V-band polarization (panel C), and the phase folded intrinsic polarization across the Balmer jump (panel D) is shown for γ Cas.

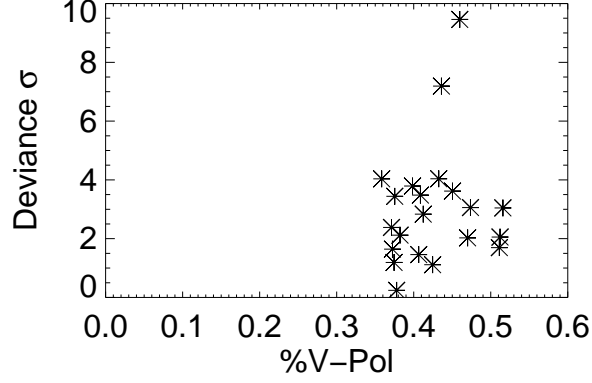


FIG. 4.— Absolute value of the error weighted deviation (deviance) of every V -band polarization of γ Cas from the best fit line defining its intrinsic disk position angle in its QU diagram (Figure 1) is plotted as a function of the magnitude of intrinsic V -band polarization present in each observation. The sporadic large deviations mimic those reported by Wisniewski et al. (2010). The online version of this manuscript includes corresponding figures for every star in our target list.

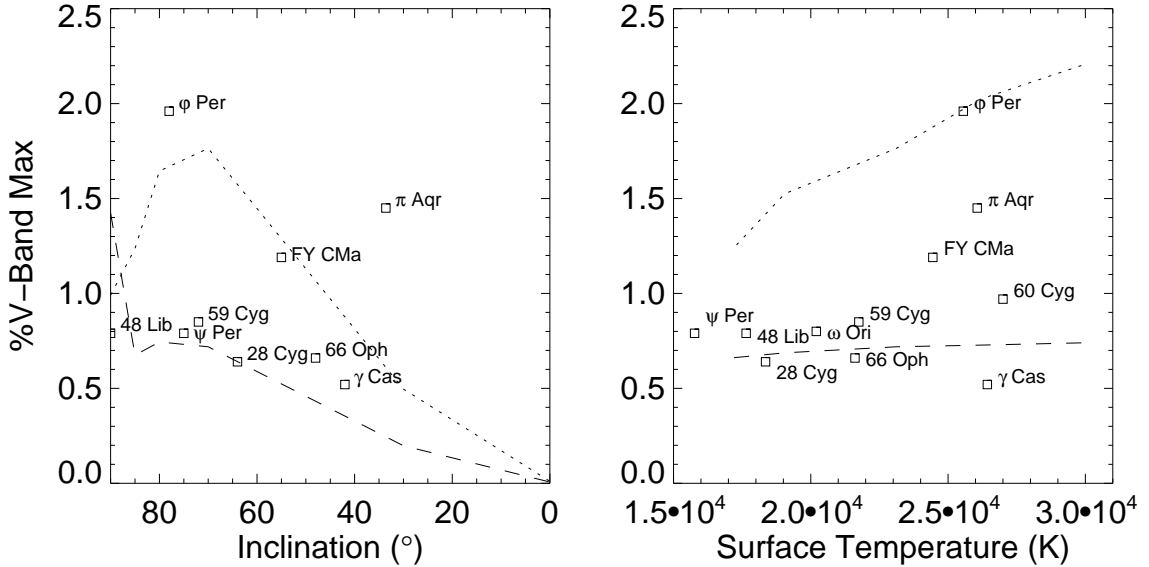


FIG. 5.— The maximum observed polarization of the target sample is plotted vs disk inclination, on the left, and effective temperature, on the right, when available. Model tracks are shown for two base densities of 8.4×10^{-12} on the dashed line and 4.2×10^{-11} on the dotted line in g cm^{-3} from Haubois et al. (2013). The model inclination tracks are of a fixed B2 type star ($T_{\text{eff}} \approx 23000\text{K}$). Inclination causes polarization to peak at $i = 70 - 80^\circ$. The model effective temperature tracks are from a fixed inclination of 70° . For low base densities, the effect on maximum polarization by effective temperature is constant where as high density models have a growing linear with higher effective temperature. The polarization maximum is degenerate between the effective temperature and inclination but general limits can be placed on the sample as a whole.